Triple structuration and enhanced corrosion performance of 316L in Laser-Powder Bed Fusion

Alexis Fouchereau, Hicham Maskrot, Fernando Lomello, Sophie Bosonnet, Oumaïma Gharbi, Benoit Gwinner, Pierre Laghoutaris, Frédéric Schuster, Vincent Vivier, Beatriz Puga

To cite this version:

Alexis Fouchereau, Hicham Maskrot, Fernando Lomello, Sophie Bosonnet, Oumaïma Gharbi, et al.. Triple structuration and enhanced corrosion performance of 316L in Laser-Powder Bed Fusion. Corrosion Science, 2024, 228, pp.111830. 10.1016/j.corsci.2024.111830 . cea-04602059

HAL Id: cea-04602059

https://cea.hal.science/cea-04602059v1

Submitted on 5 Jun 2024

Triple structuration and enhanced corrosion performance of 316L in Laser-Powder Bed Fusion

Alexis Fouchereau[a,b], Hicham Maskrot[c], Fernando Lomello[c], Sophie Bosonnet[b], Oumaïma Gharbi[a], Benoit Gwinner[b], Pierre Laghoutaris[b], Frédéric Schuster[d], Vincent Vivier[a], Beatriz Puga[b]*

[a] Sorbonne Université, CNRS, Laboratoire de Réactivité de Surface, 75005 Paris, France

[b] Université Paris-Saclay, CEA, Service de recherche en Corrosion et Comportement des Matériaux, 91191 Gif-sur-Yvette, France

[c] Université Paris-Saclay, CEA, Service de Recherche en Matériaux et procédés Avancés, 91191 Gif-sur-Yvette, France

[d] Université Paris-Saclay, CEA, Cross-Cutting Program on Materials and Processes Skills, 91191 Gif-sur-Yvette, France

GRAPHICAL ABSTRACT

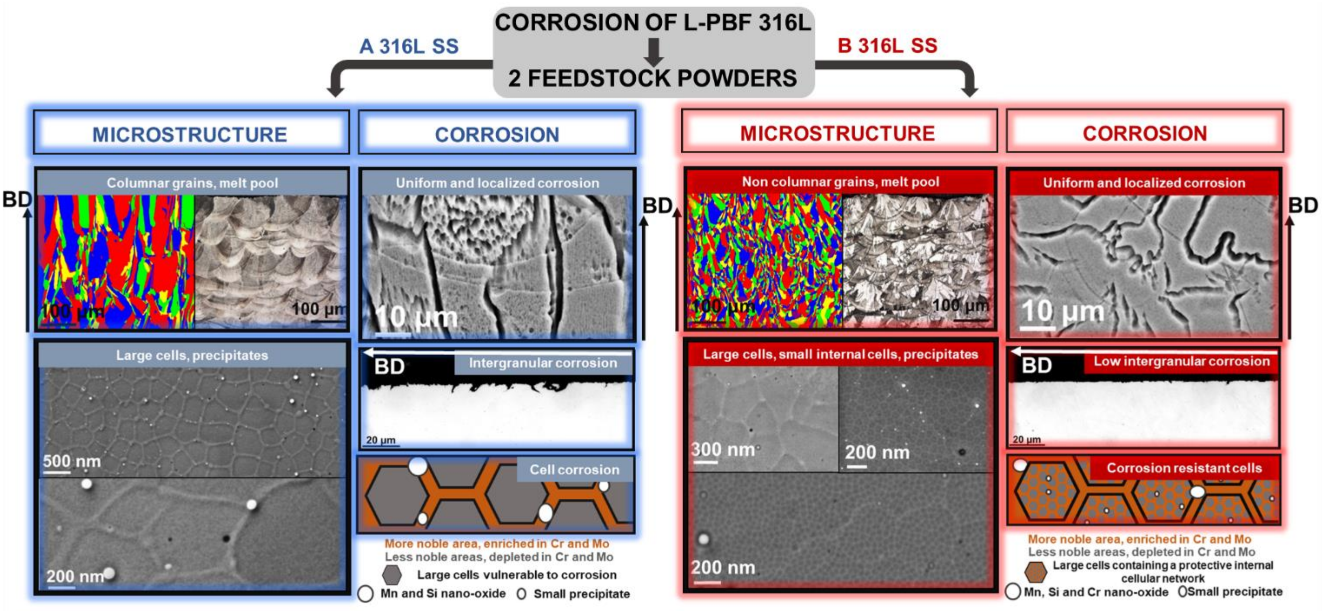

ABSTRACT

This work focuses on the influence of the feedstock powders on the microstructural properties and corrosion behavior of 316L stainless steel (SS) produced by laser powder bed fusion (L-PBF) from two different suppliers. Microstructural investigations conducted after additive manufacturing reveal many particularities depending on the powders. The first one exhibits a typical microstructure of materials obtained by L-PBF with a heterogeneous and hierarchical structure including the presence of columnar grains, precipitates of Mn and Si oxides, solidification cells (segregation in Cr, Mo and Ni), dislocations. However, the second one presents an atypical microstructure with low columnar grains growth, Mn and Si oxide precipitates which are Cr enriched and the existence of an additional small cell structure, which is organized inside the known large solidification cells. These microstructural differences lead to a different corrosion behavior in boiling nitric acid containing oxidizing ions. The presence of the triple structuration (grains, large cells, small internal cells) shows a positive effect on intergranular and cellular corrosion resistance. The existence of the smaller internal cellular sub-network allows a homogenization of the material composition and a small-scale equilibrium of the anodic and cathodic surfaces favorable to the cellular corrosion resistance. In both cases, L-PBF 316L SS provides better resistance to intergranular corrosion than wrought 316L SS which undergoes fast and severe grain loss over time.

INTRODUCTION

The development of additive manufacturing, which includes all processes that allow to manufacture, layer by layer, a physical object from a digital object, offers a series of benefits, including the ability to manufacture complex parts with specific technical characteristics, design and manufacture prototypes, customize new parts, repair objects by reducing the number of steps in the manufacturing process [1]. Technological advances in additive manufacturing finally allow to obtain a wide variety of materials and designs [2,3]. With such possibilities, additive manufacturing becomes a significant source of creativity [2,3]. In addition, some processes such as the Laser-Powder Bed Fusion (L-PBF) tend to improve profitability and production costs by recycling and reusing raw materials which are recovered in unmelted powder form [4–6].

A series of steps is previously devoted to the preparation of data and the generation of STL files and their processing [7]. The L-PBF process starts with the deposition of a thin layer of metallic powder on a substrate in a construction chamber where the atmosphere is controlled in order to limit the possible oxidation of the material [8,9]. A high energy density laser is used to scan and melt the powder bed according to the pre-selected zones of the numerical models. As a result, the powder is instantly melted and a melt pool appears [10,11]. The appearance of the melt pool and the subsequent solidification mechanism generally controls the grain structure and crystallographic texture [12,13]. A wide range of parameters (laser power, scanning speed, scanning strategy, hatching distance, powder bed thickness, building atmosphere, building orientation) controls the quality, the microstructure and the properties of the additive manufacturing products [14,15], but several types of defects can frequently be found in L-PBF materials such as porosity (lack of fusion, keyhole, gas), balling effect, surface roughness or residual stress [16–19].

In L-PBF, the material properties are also closely related to the characteristics of the feedstock powder (size distribution, shape, atomization conditions…), which determine the density and quality of the produced materials [20–23]. The challenge is to optimise the manufacturing of the raw material in order to limit the presence of any defects (internal porosity, satellites on the surface, broken particles with non-spherical shape) [24–26].

The influence of raw material properties on the microstructural characteristics of additively manufactured stainless steel has also been investigated [27]. Generally, the L-PBF 316L SS presents a columnar microstructure with highly elongated grains along the build direction (BD) [28]. The presence of melt pool together with the presence of solidification cells and a network of dislocations inside the grain were previously reported [28]. These cells result from a segregation in chemical elements (enrichment in Cr, Mo and Ni in the cell walls) and contain a high density of dislocations [29]. It has been shown that suitable parameter combinations can modify the overall microstructure of the steel, by applying a specific scanning strategy with particular rotation angles, epitaxial and columnar grain growth can be inhibited resulting in a material with an equiaxed grain morphology [30]. Moreover, depending on the raw material manufacturing route, different microstructures were observed [27], but the mechanisms of equiaxed/cellular growth and their correlation with the raw material are yet to be elucidated.

From a practical point of view, manufacturing process should guarantee performance levels at least equal or higher than those obtained with conventional materials. However, in the literature some inconsistencies have been pointed out. For instance, a lower corrosion resistance has been reported for L-PBF 316L SS [31–34], which can be assigned to the presence of porosities on the surface of the material. Conversely, the corrosion resistance of L-PBF 316L SS can be improved thanks to the removal of MnS precipitates in L-PBF [35–40], whereas a more stable and extended passive range than conventional SS [41] has also been reported, which was a consequence of the refined microstructure obtained in L-PBF due to a reduce diffusion path of chromium [41]. Most of the studies have focused on the pitting behavior of L-PBF 316L SS in environments containing chlorides [33,42]. Nevertheless, few studies have focused on the behavior of L-PBF 316L SS in a complex and strongly oxidizing acidic medium such as nitric acid [43,44]. Under these conditions, SS is in its passive domain where it shows a slow and uniform dissolution ascribed to the formation of a protective, stable and adherent oxide layer, which is a few nanometers thick and mainly composed of chromia, Cr_2O_3 [45,46]. However, strong oxidizing media can shift this corrosion potential into its transpassive domain, thus developing a dissolution faster than in the passive domain and developping localized corrosion, especially at the grain boundaries of the material (intergranular corrosion). Acceleration of dissolution is due to a change of the mean oxidation degree of Cr, from III in the passive domain (forming protective species such as Cr_2O_3) into VI (forming soluble species) in the transpassive domain [45,46].

Moreover, intergranular corrosion can develop until grains dissociate from the surface, which significantly increases the damaging of the material [47]. The most common example of intergranular corrosion concerns sensitized SS, which have been heat-treated in the temperature range of 500°C to 700°C (during a welding operation or an ageing phase, for example). During this sensitization process, chromium carbides (typically $Cr_{23}C_6$) formed at the grain boundaries [48] leading to chromium depleted zones around the grain boundaries, which are less protective against corrosion. The second case of intergranular corrosion occurs even for non-sensitized steels (the formation of chromium carbides can be avoided by suitable heat-treatments and the lowering of the C content, typically < 0.03 wt.%), when the SS is in its transpassive domain in a strong oxidizing environment [47–50].

In the case of new manufacturing processes which lead to a specific microstructure, it thus appears essential to characterize these innovative materials, since only few works have reported on the corrosion behavior of these materials in acidic media. In such aggressive environments, it can be expected that some microstructural specificities (cells, dislocations, residual stresses, grain morphology and size, texture...) influence the behaviour of the material. Regarding the microstructural variabilities generated in additive manufacturing, the understanding of the influence of the raw material on the properties of L-PBF 316L SS is also required. One of the challenges is to understand how 316L SS powder, as a raw material, can influence the solidification mechanisms and properties of L-PBF 316L SS. Thus, this study focuses on the relationship between the microstructure and the corrosion behavior in strongly oxidizing nitric acid at boiling temperature. The performances of these materials are also compared to conventional wrought 316L SS.

RESULTS AND DISCUSSION

Microstructure and nanostructure characterizations

A comparison of the XRD diagrams obtained for the three materials is presented in Fig. 1. For the A and B 316L SS, only the austenitic phase is observed without the presence of a ferritic phase, in agreement with the literature [43]. On the other hand, the wrought 316L SS shows a slight peak corresponding to ferrite (110) planes which reflects the existence of a ferritic phase. The presence of ferritic phase for the wrought 316L SS is ascribed to the slow cooling rate during the manufacturing process [51,52]. Moreover, relative intensities of austenite peaks are similar for the three materials. They do not highlight strong texture.

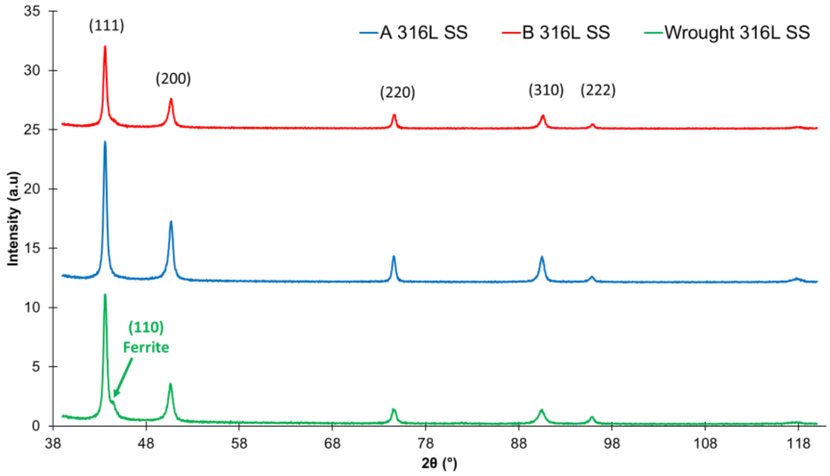

Fig. 1: XRD diagrams obtained on the 316L SS (paralell to BD for L-PBF 316L SS).

The analyses obtained by electron backscatter diffraction (EBSD) on the wrought 316L SS are shown in Fig. 2. The wrought 316L SS presents a homogeneous microstructure with equiaxed grains and an average size of 46 µm (Fig. 2.A). The morphology of the equiaxed grains is also related to a low crystallographic texture and anisotropy (Fig. 2.B). Moreover, the EBSD area shows an inhomogeneous distribution of grain boundaries according to their disorientation angle (Fig. 2.C). Indeed, within the wrought 316L SS, we notice a major quantity of ∑3 twin boundaries (53.9%), a significant quantity of High Angle Grain Boundaries (HAGB > 10°, 45.6%), and a very low quantity of Low Angle Grain Boundaries (LAGB < 10°, 0.5%). The precipitates present in the wrought 316L SS are specific to the conventional manufacturing process and solidification mechanisms. In the literature, these precipitates have been described as MnS [53].

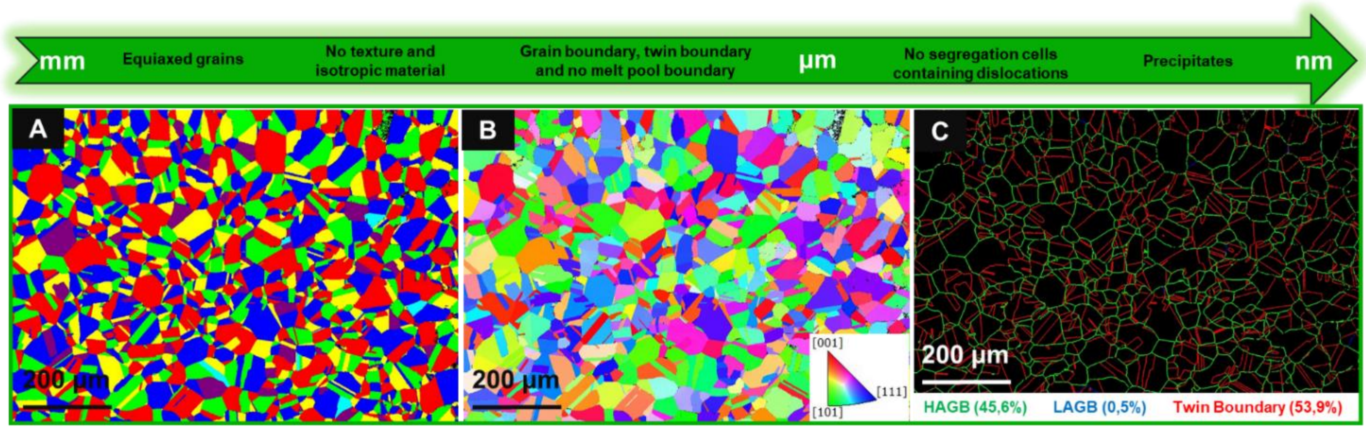

Fig. 2: Homogeneous structure and equiaxed morphology of wrought 316L SS studied by EBSD – (A): EBSD map of grains. (B): IPF parallel to the build direction. (C): Map of the grain boundaries.

Concerning the L-PBF 316L SS, similarities and major differences were observed in the microstructural analyses. The similarities between A and B 316L SS reside in the hierarchy of their microstructure, which has already been highlighted in the literature and is due to the rapid solidification induced by the additive manufacturing process [54]. However, important and unexpected differences have been observed at different scales. For A 316L SS, optical micrographies (Fig. 3.A) highlight the presence of melt pool (whose average depth is about 83 µm) and columnar grains elongated and parallel to the build direction. The columnar grains on Fig. 3.B have an average size of 48 µm, which were formed by epitaxial grain growth [55]. Thus, the preferential crystallographic direction of these columnar grains corresponds to the solidification trajectory described as parallel to the maximum thermal gradient direction [55]. Under these conditions, for a single melt pool which solidifies along the build direction, grains with <100> orientation will preferentially grow from the bottom of the melt pool toward its center. Also, due to the shape of the melt pool (grains at the edge of the <100> bath are oriented at 45° to the build direction) and the remelting associated with the adjacent laser pass, the grains formed in the remelted area will tend to be <110> oriented. Concerning the grain boundaries inside the A 316L SS, a different distribution of their disorientation angles compared to the wrought 316L SS is observed, with a majority of HAGB (74.7%), a significant amount of LAGB (24.6%) and a very small amount of $\sum 3$ twin boundaries (0.7%). In the literature, the L-PBF process has already shown to form more LAGB than traditional steel [54]. At a smaller scale, inside the grains, solidification cells were observed (Fig. 3.C and Fig. 3.D), which have an average size of 376 nm. These cells are characterized by nanostructures that can be seen as sub-grain boundaries, precipitates and a high dislocation density. Qualitative and quantitative local chemical composition analyses were thus performed by STEM/EDX (Fig. 3.C) and showed enrichments in Cr of 0.8 ± 0.54 wt.%, and in Mo of 0.6 ± 0.36 wt.% at the cell walls compared to the average composition of the material. Furthermore, the analysis of precipitates also confirms the presence of Mn and Si oxide precipitates, typical of 316L SS produced by L-PBF [29]. Finally, SEM observations on thin sections (Fig. 3.D) allow a better observation of the distribution and the size of precipitates in this cellular network. Two kinds of precipitates can be identified: a population of large precipitates with an average diameter of about 69 nm and another one with an average diameter of 19 nm. These observations also suggest that the precipitates tend to localize preferentially at the cell walls but some precipitates can also be found inside the cell matrix. Concerning the dislocations (Fig. 3.C), they result from the thermal gradient and the rapid solidification during the L-PBF process [56,57]. According to [58], regions containing a high dislocation density tend to be Cr-enriched, leading to solute depletion. In this case, the dislocation network exacerbates the formation of chemical heterogeneities at the same locations. In the case of A 316L SS, the dislocations are mainly located at the cell walls but some dislocations are also observed inside the cells.

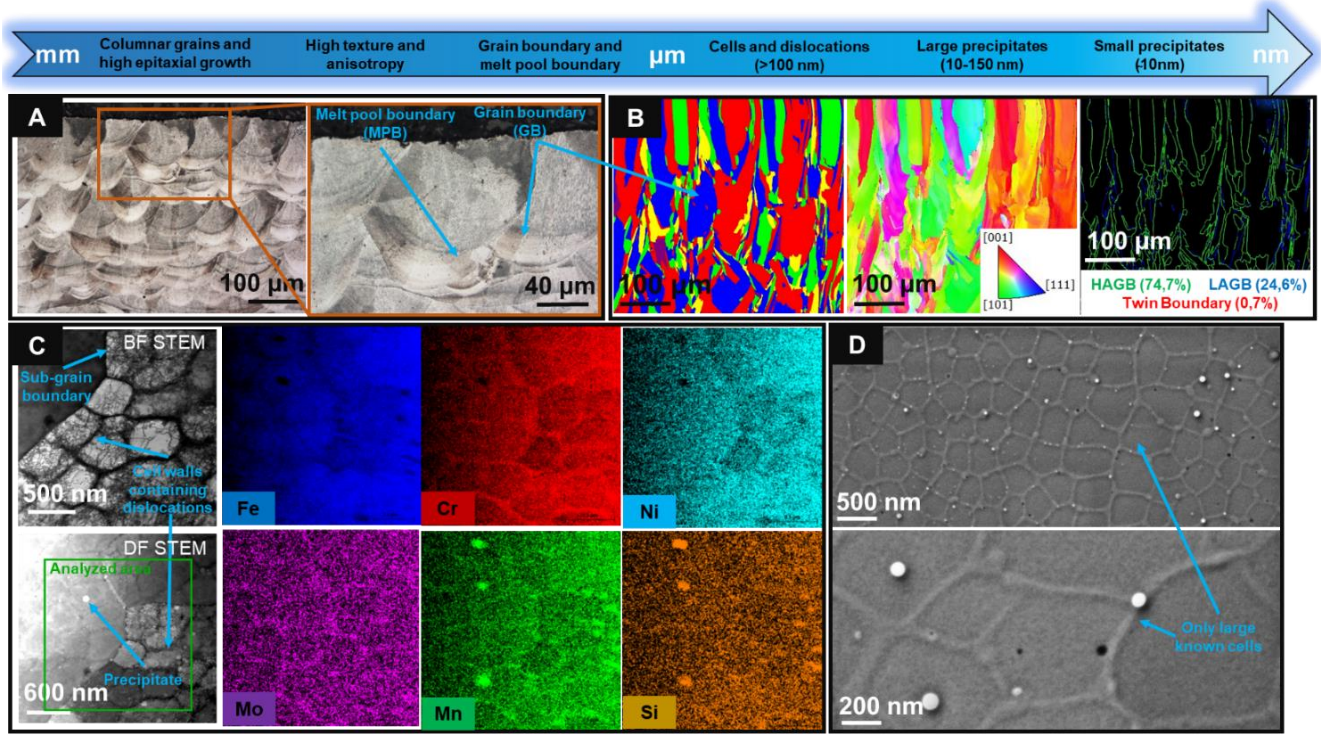

Fig. 3: Heterogeneous and hierarchical structure of A 316L SS (parallel to BD) – (A): Optical micrographies after chemical etching with oxalic acid. (B): EBSD map of grains, IPF and grain boundaries. (C): STEM observations of precipitates, cells, dislocations and STEM/EDX mapping in Fe, Cr, Ni, Mo, Mn, Si. (D): Cells and precipitates by SEM on thin sections.

Melt pool has also been observed by optical microscopy after electrochemical etching in oxalic acid on B 316L SS (Fig. 4.A), Its average depth is about 79 µm. Nevertheless, the grains do not seem to grow through the successive melt pool as before. This trend is confirmed in Fig. 4.B, where smaller grains (on average 26 µm) are observed. It is very likely that this atypical morphology of grains is related to an inhibition of epitaxial grains growth, itself induced by the specific properties of the raw material (chemical composition, atomization, internal structures already existing in the powder...). Moreover, the inhibition of epitaxial and columnar grain growth decreases the structural anisotropy of the material. The distribution of grain boundaries shows a majority of HAGB (74.2%), whereas the quantity of ∑3 twin boundaries is about 17.2% with a significant decrease of the amount of LAGB (8.6%) compared to A 316L SS. Additionally, solidification cells appear inside the grains, as shown in Fig. 4.C and Fig. 4.D, the size of which are about 385 nm. Local chemical composition analyses (Fig. 4.C) show the same trend as A 316L SS. The cell walls show enrichments in Cr of 0.9 ± 0.34 wt.% and in Mo of 0.6 ± 0.3 wt.% compared to the average composition of the material. Concerning the precipitates, the main difference is that the Mn and Si oxides also seem to be Cr enriched for the B 316L SS (enrichment of 0.8 ± 0.6 wt.%). These oxide precipitates which are enriched in Cr, Mn and Si could play a role in the inhibition of grains columnar growth. Finally, the most important difference between the L-PBF 316L SS is presented in Fig. 4.D. Indeed, the SEM observations on the B 316L SS thin sections have revealed the existence of a cellular sub-network within the large cells previously described. The small cells of this sub-network have an average size of 30 nm and are organized in a very regular pattern inside the large solidification cells. For the B 316L SS, the hierarchical structure of the material is even more pronounced with the existence of an unexpected triple structuration (grains, large cells, small internal cells). To this triple structuration is also added an important density of small precipitates whose size is on average 9 nm and which are mostly located at the borders of the internal small cells (Fig. 4.D). The quantity of these small precipitates is more important than in the A 316L SS. It is hypothesized that these numerous small specific precipitates come from the raw material and could play a role in the formation and stabilization of the internal cellular sub-network. As for the dislocation network in B 316L SS, it seems to be more localized and concentrated in the wall of the large cells compared to A 316L SS. This localization at the large cell wall could be related to the presence of the small internal cell sub-network which pushes the dislocations to the frontier of the large cells.

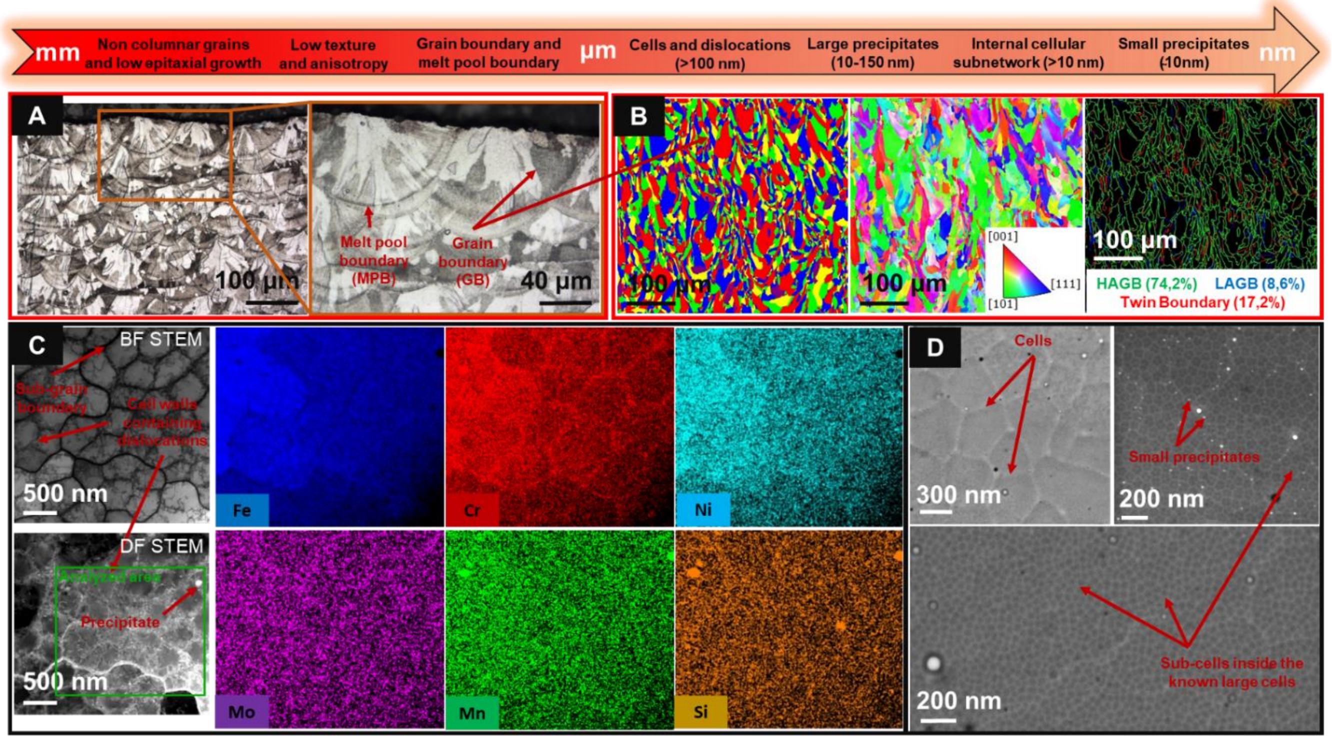

Fig. 4: Hierarchical structure of B 316L SS (parallel to BD) – (A): Optical micrographies after chemical etching with oxalic acid. (B): EBSD map of grains, IPF and grain boundaries. (C): STEM observations of precipitates, cells, dislocations and STEM/EDX mapping in Fe, Cr, Ni, Mo, Mn, Si. (D): Large and small internal cells and precipitates by SEM on thin sections.

Immersion test

The corrosion behavior of 316L SS was investigated in boiling nitric acid solution (5 mol.L^{-1} HNO_3) containing V(V) (4.10^{-3} mol.L^{-1}) as oxidazing agent. The materials studied here did not receive any post-treatment after their synthesis. The low C content (< 0.03 wt.%) of these steels avoids the formation of Cr carbides at the grain boundaries and prevents intergranular corrosion related to a localized depletion of Cr.

Evolution of the surface morphology observed *ex situ* by optical microscopy and mass loss measurements of 316L SS are presented as a function of time in Fig. 5. The mass loss was normalized from the initial geometric surface of the samples. First, the mass loss kinetics is different for the 3 materials. Both L-PBF 316L SS show a rather linear evolution of the mass loss which could reflect stationary and uniform corrosion process. Conversely, for the wrought 316L SS, the mass loss kinetics is not linear and has more a parabolic trend. This behaviour is typical of a SS (with a isotropic grain structure) suffering from intergranular corrosion (IGC) in a strongly oxidizing and boiling nitric medium [47]. After 240 h in solution, the less performing steel is clearly the wrought 316L SS which presents a mean corrosion rate of 191 ± 14 µm.year^{-1} over the whole test duration (calculated from the cumulative mass loss of 357 ± 15 mg.dm^{-2} at the end of the immersion test and assuming a uniform dissolution of the surface). This is twice higher than for steels obtained by additive manufacturing. During the first 150 h of corrosion, the two additive manufacturing steels show equivalent corrosion rates (the cumulative mass-loss of the B 316L SS being slightly lower than the one of the A 316L SS). However, after 150 h, we observe a significant increase of the mass loss of the A 316L SS, which corresponds to an intensification of the attack at the grain boundaries. But conversely to the wrought 316L SS, no grain loss was observed after 240 h of immersion (Fig. 5.B). The average cumulative mass-loss finally reaches 138 ± 3 mg.dm^{-2} for B 316L SS, versus 160 ± 2 mg.dm^{-2} for A 316L SS, which correspond to corrosion rates of 70 ± 2 µm.year^{-1} and 83 ± 4 µm.year^{-1}, respectively. In reality, this analysis underestimates the actual corrosion rate, which is greatly exacerbated in the presence of severe intergranular corrosion and grain loss, as illustrated by the photos after different stages of immersion (Fig. 5.B). However, significant differences in corrosion morphology are observed between A and B 316L SS (Fig. 5.B). In the case of A 316L SS, increasingly darker areas appear on the surface and add to the grain boundary attacks, suggesting the emergence of another localized corrosion morphology on the surface, whereas for B 316L SS, these dark areas do not appear and only grain boundary attack occurs. The slightly higher mass loss for B 316L SS during the first periods of immersion could be related to microstructural differences. Indeed, it is important to remember that B 316L SS has a smaller grain size and a higher density of grain boundaries on the surface. Under these conditions, the increase in grain boundary density could be unfavorable in an environment where the dissolution kinetics of the grain boundaries occurs preferentially and is higher than in the grain itself.

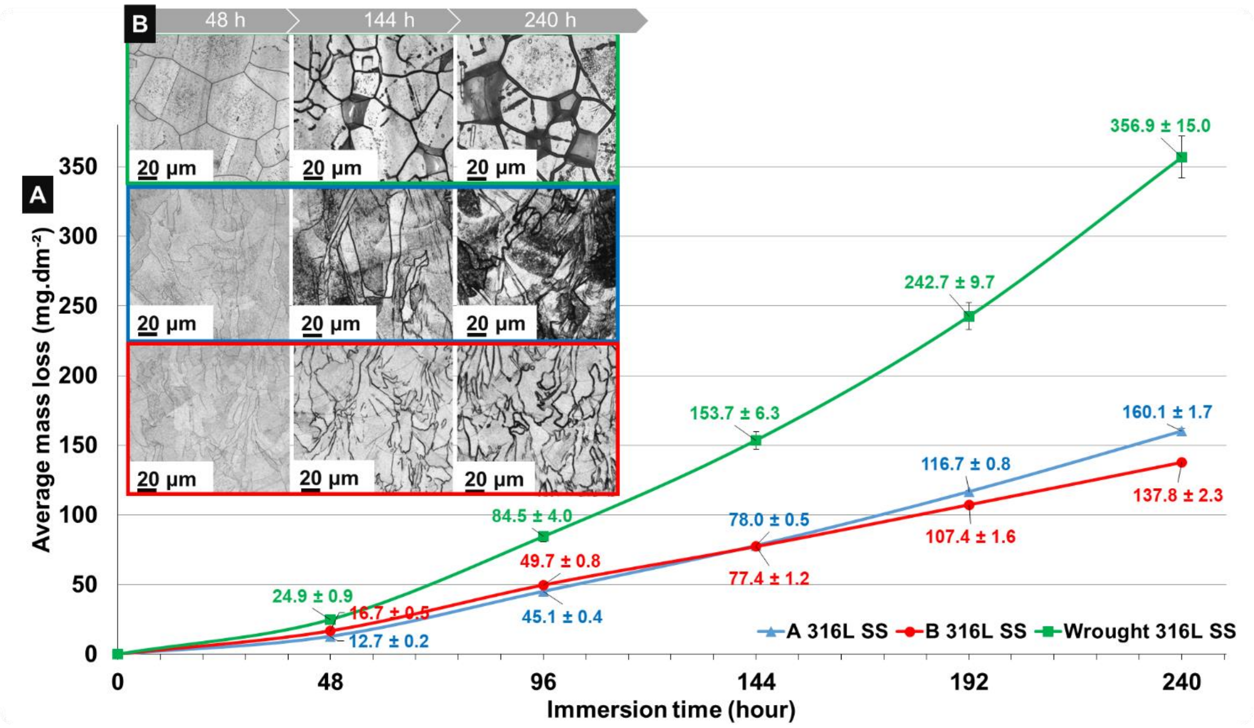

Fig. 5: (A): Average mass loss of wrought 316L SS, A 316L SS and B 316L SS as a function of immersion time normalized by the initial geometric surface. (B): Optical microscopy observations of the surface of wrought 316L SS, A 316L SS and B 316L SS after 48 h, 144 h and 240 h of immersion in nitric acid containing V(V) at boiling temperature.

Finer characterizations were performed by SEM observations and by interferometric microscopy (Fig. 6). For wrought 316L SS, Fig. 6.A and B confirm the grain boundary attack and surface grain detachment described above, as well as a shallower intergranular penetration depth at the twin boundaries compared to the other grain boundaries. This observation is in agreement with the literature which has shown that the corrosion rate depends on the nature of the grain boundary [47]. Therefore, twin boundaries are more resistant than LAGBs, which are themselves more resistant to intergranular corrosion than HAGBs [47]. Concerning A 316L SS, Fig. 6.C and D highlight the nature of the attacked structures located at the dark zones previously described in Fig. 5. These dark areas correspond to a localized attack in the solidification cells when these are oriented perpendicularly to the surface of the material and for which the Cr and Mo contents are the lowest.

According to [59,60], the cell walls and matrices together form a galvanic coupling characterized by more noble cathodic zones corresponding to the cell walls and less noble anodic zones corresponding to the cell matrices. This behavior is related to the difference in Cr and Mo composition in the cell structures [59,60], and is also responsible for a significant increase in the surface roughness of the material (Fig. 6.D).

SEM and interferometric characterizations confirm the existence of an unexpected corrosion behavior for B 316L SS (Fig. 6.E and F). Indeed, this material shows a low surface roughness after corrosion (Fig. 6.F), in relation with an increased resistance to cellular corrosion described previously. This increased cell corrosion resistance is explained by the presence of a cellular sub-network within the large cells. The small cells in this sub-lattice (average size 30 nm) also consist of a wall and a matrix that are organized within the large cell matrix known for L-PBF 316L SS. It is assumed that the arrangement of the small internal sub-cells increases the surface density of the cell walls within the large cells. Their arrangement and organization then induce a significant reduction in the surface area corresponding to the cell matrices and the anodic surface. It is deduced that the existence of this internal cellular sub-network allows a homogenization of the material composition and a balance on a smaller scale of the anodic and cathodic surfaces favorable to the corrosion resistance of the B 316L SS.

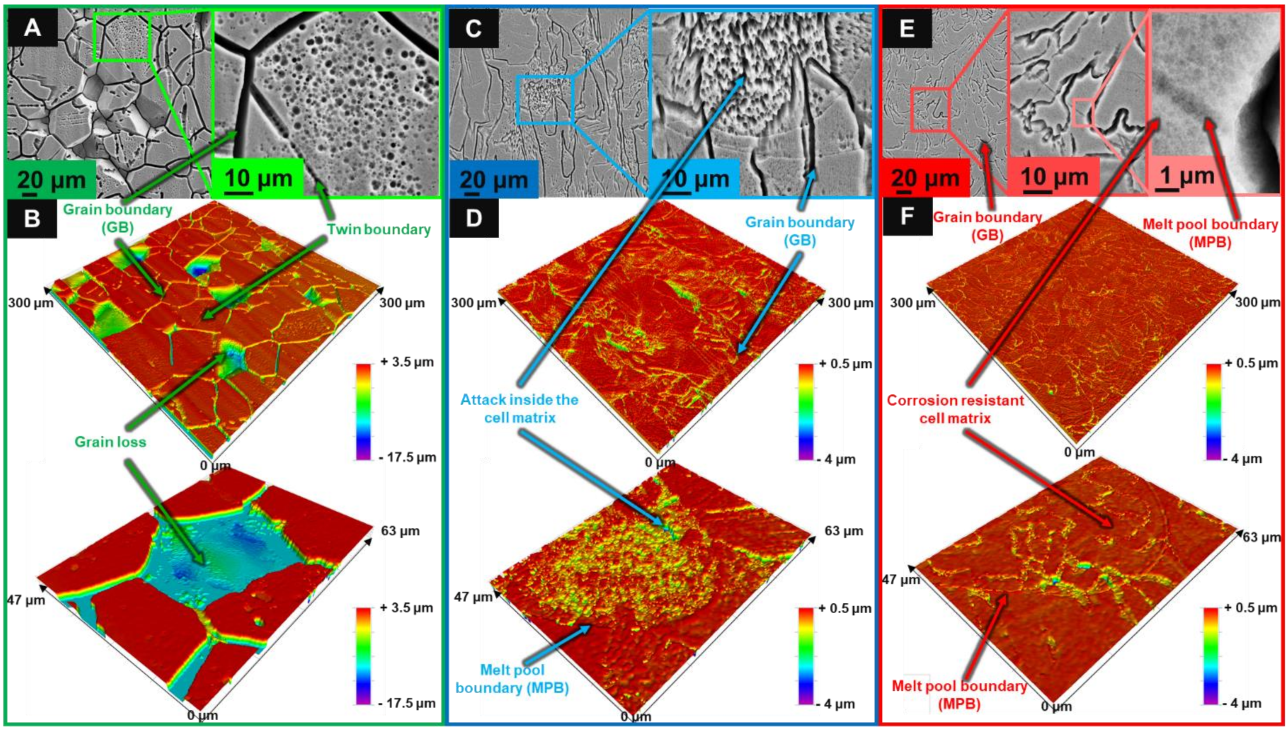

Fig. 6: Observations of the corrosion morphologies after 240 h of immersion in nitric acid containing V(V)at boiling temperature for 316L SS samples – (A),(C),(E): SEM observations at different magnifications respectively for the wrought, A and B 316L SS. (B),(D),(F): Optical profilometer observations respectively for wrought, A and B 316L SS.

Moreover, it has been shown in the literature, from SEM and scanning Kelvin probe force microscopy (SKPFM) analysis that the size of the solidification structures could have an influence on the detected signal [60]. Indeed, according to [60], the surface work function is closely related to the concept of Volta-potential. Thus, when the cell size increases, the potential difference between the anode and the cathode also increases, which corresponds, for a corrosion experiment, to an increase of the driving force for galvanic corrosion.

Cross-sectional observations of the materials were also performed by optical microscopy (Fig. 7). They show significant differences for the localized attack depth at the grain boundaries: the wrought

316L SS has deep intergranular grooves and high attack angles (Fig. 7.A). This observation explains the significant grain loss described above for this steel after several days of immersion in an aggressive environment. It is also observed that for B 316L SS, the depth of the intergranular grooves is very low (Fig. 7.C), which reflects a real improvement of the intergranular corrosion resistance for this material, even when compared with A 316L SS (Fig. 7.B).

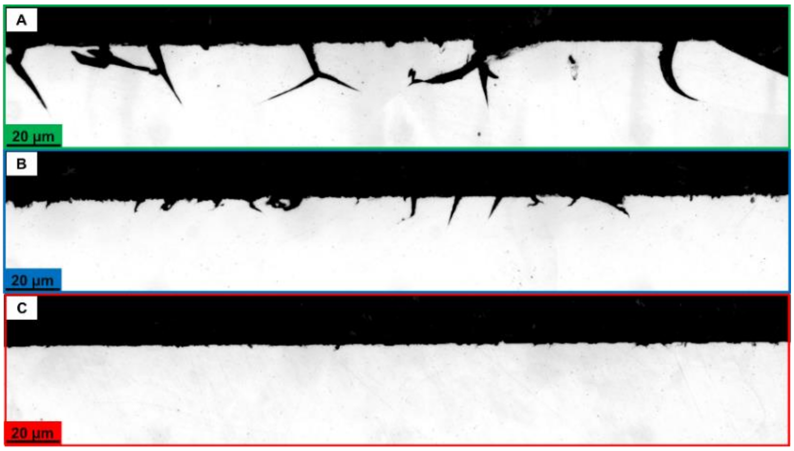

Fig. 7: Cross-sectional observations by optical microscopy after 240 h of immersion in nitric acid containing V(V) at boiling temperature for – (A): Wrought 316L SS, (B): A 316L SS and (C): B 316L SS.

In addition, depending on the material, intergranular and cellular corrosion occurs to a varying degree, leading to a different increase in surface area.This increase in surface area called R_{corr} (that means the ratio of the corroded surface area (S_{corr}) to the initial surface area (S_{ini})) was measured at the end of 240 h of immersion from several cross-sectional observations as in Fig. 7. The same ratio has been then estimated for intermediate immersion times by interpolation between 0 and 240 h considering a linear increase of the surface area over time [50]. This assumption of a linear increase of the surface is in agreement with the experimental and modelled behaviour observed for a SS surfering IGC. Interpolated values are presented in Table 1:

Table 1: Evolution of R_{corr} (the ratio of the corroded surface area (S_{corr}) to the initial surface area (S_{ini})) for immersion time in nitric acid containing V(V) at boiling temperature (measured at 240 h and interpolated between 24 and 192 h).

	R_{corr}					
Immersion time (h)	24	48	96	144	192	240
Wrought 316L SS	1.14	1.28	1.57	1.85	2.15	2.42
A 316L SS	1.07	1.14	1.27	1.41	1.55	1.69
B 316L SS	1.01	1.03	1.05	1.09	1.11	1.14

XPS analyses were performed to compare the chemical composition of the oxide layer formed above these three materials. They show that there is no significant difference in the oxide layer chemical composition, since it is mainly composed of Cr(III) (proportion of cations about 90 ± 3 at.%) with a small amount of Fe(III) (approximately 8 ± 2 at.%) and Mo(VI) (approximately 2 ± 1 at.%). The nature of the oxide layer alone does not explain the differences in behavior towards intergranular corrosion. Nevertheless, the results obtained here did not allow us to compare their thicknesses, or their structures.

Electrochemical analysis

In order to better understand the evolution of these different stainless steels and their surface properties, electrochemical experiments were performed. The electrochemical results of this study have been normalized from the real surface of the materials during the immersion time. Indeed, the evolution of the electrochemical properties (oxide thickness, surface reactivity...) and the surface area influence the impedance response. In order to focus only on electrochemical properties of the materials, the real corroded surface (S_{corr}) is used to normalize the electrochemical measurement results. Using the values given in Table 1, S_{corr} was obtained as the function of the immersion time using the following equation (1)

$$S_{corr} = S_{ini}.R_{corr} \qquad (1)$$

Linear voltammetry experiments were carried out at the end of the 240 h of immersion and the current density was plotted as a function of the potential in a Tafel representation (Fig. 8). The corrosion potential is almost equivalent for the three materials with a value close to 0.45 V/MSE. The shape of the anodic curves and the very significant increase in current density with the potential indicate that the metals have a corrosion potential close to the beginning of the transpassivity. A small anodic overvoltage is sufficient to make the materials enter abruptly in the transpassive domain corresponding to the oxidation of insoluble Cr(III) (present in Cr_2O_3 in the passive layer) into soluble Cr(VI) (present in $Cr_2O_7^{2-}$ in solution).

When a potential scan is applied in the cathodic domain of the material, the reduction of the medium is favored over the oxidation of the material. Indeed, it should be remembered that the global current measured (by electrochemistry) is the sum of both the cathodic and the anodic current. The actual anodic contribution can be obtained by an additional measurement of the dissolution of the material, for example by measuring the mass loss kinetics [46] or analyzing the evolution of the corrosion products in solution [61].

For low cathodic overvoltages, an increase in current density is observed which is similar between materials. The reduction kinetics is strongly dependant on the reactions involved but also on the presence of the oxide layer on the surface that governs the electrons availabity for the cathodic reactions at the oxide/solution interface [45]. The similarity in the cathodic current density between all materials could be due to an oxide layer presenting close properties in terms of reactivity. The fact that both cathodic and anodic current densities are equivalent for the three materials leads to obtain here an almost similar corrosion current (J_{corr}) with a value close to 10 µA.cm^{-2}.

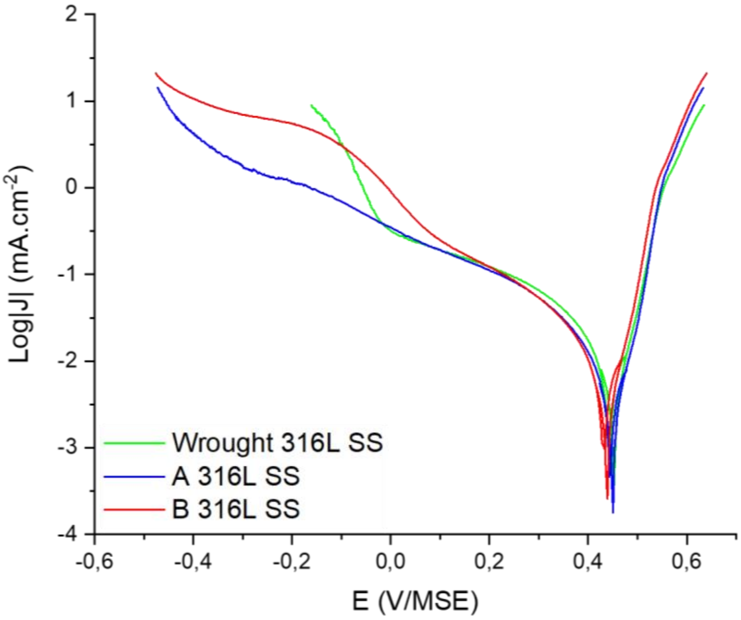

Fig. 8: Linear voltammetries obtained for 316L SS at 240 h of immersion with a scan rate of 0.2 mV.s^{-1} in nitric acid containing V(V) at boiling temperature. The results are normalized by the real corroded surface (S_{corr}).

Electrochemical impedance measurements were performed at different immersion times in order to characterize and compare the properties of the passive layer formed on the alloys. The impedance diagrams presented in Fig. 9.B-D suggest the presence of a single time constant, a capacitive loop. In the case of a passive system, the impedance of electrochemical systems often reflects a distribution of time constants which can be represented in equivalent electrical circuits by a constant-phase element (CPE) [62], which can be interpreted as a distribution of its resistive properties along its thickness. The CPE impedance expresses as [63]

$$Z_{CPE} = \frac{1}{Q(j\omega)^{\alpha}} \qquad (2)$$

with Q and α defined as the parameters of the CPE, which can be readily obtained from a graphical analysis [64]. A different approach to the use of equivalent circuits has shown that a power law model (PLM) can describe the behavior of a passive film [65,66]. This physical description of the system assumes, on the one hand, that boundary values for the resistivity at both interfaces metal/oxide and oxide/electrolyte apply, and on the other hand, that the dielectric constant is uniform and constant throughout the passive film. Thus, the resistivity distribution along the oxide film expresses as [65,66]

$$\frac{\rho}{\rho_\delta} = \left(\frac{\rho_\delta}{\rho_0} + \left(1 - \frac{\rho_\delta}{\rho_0}\right)\xi^{\gamma}\right)^{-1} \qquad (3)$$

$$\gamma = \frac{1}{1-\alpha} \qquad (4)$$

With ρ_0 and ρ_δ which are the resistivity at the metal/oxide and oxide /electrolyte interface, respectively. Using the PLM it is also possible to estimate the thickness δ of the oxide layer according to

$$\delta = \frac{(\varepsilon\varepsilon_0)^\alpha}{gQ\rho_\delta^{1-\alpha}} \qquad (5)$$

where g is a parameter defined as

$$g = 1 + 2.88\left(\frac{1}{1-\alpha}\right)^{-2.375} \qquad (6)$$

Assuming $\varepsilon = 12$, which corresponds to the dielectric constant of Cr_2O_3 and Fe_2O_3 [67] and $\rho_\delta = 450\,\Omega$.cm [66], corresponding to the typical value of a semiconductor, it is possible to obtain an approximate value of the oxide thickness. Finally, it is also possible to determine the oxide film capacitance from the expression [68]

$$C_{PLM} = gQ(\rho_\delta\varepsilon\varepsilon_0)^{1-\alpha} \qquad (7)$$

Experimental impedance measurements were fitted with the equivalent circuit presented in Fig. 9.A, and the results are presented in Table 2 and Fig. 9. The equivalent circuit presented here has been chosen to model the global behavior of the metal/oxide/electrolyte interface. In this equivalent circuit, we find R_e which corresponds to the electrolyte resistance, R_{elec} corresponding to the electronic resistance in the oxide film, R_{ct} corresponding to the charge transfer resistance at the oxide/electrolyte interface responsible of the cathodic reaction, C_{PLM} associated to the oxide film capacitance in relation with the power law model and the resistivity distribution, Q_{dl} and α_{dl} corresponding to the capacitive behavior of the electrochemical double layer. It should be noted that this circuit does not allow to determine independently R_{elec} and R_{ct}, and in practice, only a single resistance is obtained which is the sum of these two contributions. According to the equivalent circuit, the double layer capacitance and the oxide film are in series. However, in this study, the double layer capacitance has been neglected, considering that the capacitance values obtained for a double layer are generally close to 50 µF.cm^{-2}, which is much higher than the values obtained for an oxide capacitance [69].

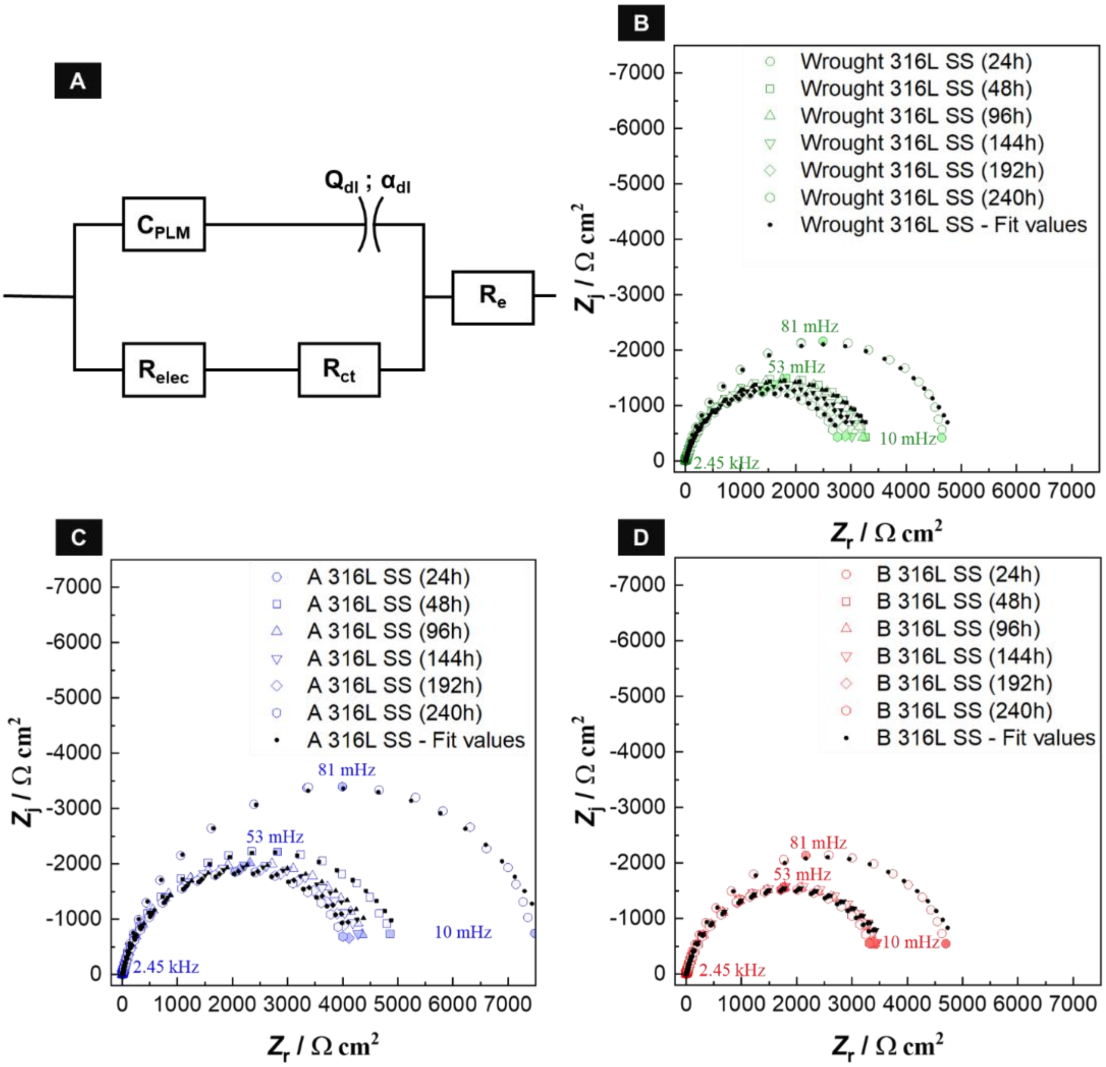

Fig. 9: A: Electrical equivalent circuit (EEC) describing the interface formed by the alloys with the electrolyte; B, C, D: Nyquist representations of electrochemical impedance measurements obtained for the 316L SS at different immersion times (24 h, 48 h, 96 h, 144 h, 192 h, 240 h) in nitric acid containing V(V) at boiling temperature. The results are normalized by the real corroded surface (S_{corr}).

First, the CPE parameters α, Q and the electrolyte resistance (R_e) were obtained by graphical determination from the experimental results without adjustment. To simplify the fitting, the values obtained by graphical determination for α, Q and R_e have been previously fixed. From the fit, it was possible to determine the electronic resistance in series with the charge transfer resistance (R_{elec} + R_{ct}) and the resistivity at the metal/oxide interface (ρ_0). Here, even if the evolution of R_{elec} + R_{ct} seems close from one material to another, it is possible to observe that the values obtained for A 316L SS are higher than B 316L SS, themselves slightly higher than the values obtained for wrought 316L SS. The results being normalized by the real corroded surface, they do not take into account the aggravation of the corrosion rate induced by the localized corrosion and the progressive increase of the surface. Concerning the values of ρ_0, they vary between 10^9-10^{10} Ω.cm, which corresponds to a typical resistivity for an insulator.

From the CPE parameters, it was possible to solve equations (5) and (7) to identify the evolution of the oxide film thickness δ (nm) and capacitance C_{PLM} (μF.cm^{-2}) respectively. At the end of the test, the δ and C_{PLM} values obtained are not significantly different between the materials and therefore do not explain the differences in corrosion performance. In addition, the oxide thickness values obtained are small and have an order of magnitude smaller than those for passive layers observed on other steels in nitric media. It is likely that this small oxide thickness is related to transpassivity. Despite close values of thickness and oxide capacity for wrought 316L SS compared to A and B 316L SS, this one remains the least performing regarding the mass loss. Indeed, we remind that severe intergranular corrosion develops on the surface of wrought 316L SS. Considering the results obtained in electrochemistry and also in XPS, this increased sensitivity to intergranular corrosion is therefore not related to the nature and the properties of the oxide layer. It is probable that the rapid intergranular dissolution for this material is related to the intrinsic properties of the grain boundary (chemical composition, effect of impurities). Considering the significant differences in solidification rates according to the process used, it is possible that the difference in the intergranular corrosion resistance is mainly related to a different chemical segregations at the grain boundaries according to the cooling rates. Also, the performance comparison between A and B 316L SS could not be explained by the surface oxide layer. More precisely, even if in both cases, the L-PBF materials present a quasi-linear mass loss and an absence of loss of grains at the surface, an improvement of the intergranular and cellular corrosion resistance is obtained for B 316L SS. The enhancement of grain boundary resistance of this material could be related to the lower impurity content (especially for P and S) in the raw material composition leading to a lower segregation. In addition, the existence of an unexpected triple structuration (grains, large cells, small internal cells) may guarantee a protection against cellular corrosion of L-PBF materials. In this case, the corrosion observed for the B 316L SS can be considered as uniform allowing in theory a better surface stability over time. Since the electrochemical measurements performed in this study reflect the global behavior of the materials, it is possible that differences exist locally in the oxide layer. Indeed, for B 316L SS, the triple structuration and the uniform corrosion highlighted could induce a homogeneous and less defective oxide layer on its entire surface. On the contrary, for A 316L SS, the high sensitivity to cellular corrosion could initiate locally the appearance of defects and inhomogeneities within the oxide layer.

Table 2: Results obtained from the impedance measurements for 316L SS as a function of time in nitric acid containing V(V) at boiling temperature. The results are normalized by the real corroded surface (S_{corr}).

	Immersion time (h)	**α^a**	**Q^a (μF.cm^{-2}.s$^{1-\alpha}$)**	**R_e^a (Ω.cm^2)**	**C_{PLM}^b (μF.cm^{-2})**	**δ^b (nm)**	**$R_{elec}+R_{ct}^c$ (Ω.cm^2)**	**ρ_0^c (Ω.cm)**
Wrought 316L SS	24	0.855	420	1.65	19.2	0.55	4971	4.10^9
	48	0.814	842	1.80	16.4	0.65	3565	7.10^9
	96	0.812	880	1.96	16.4	0.65	3529	7.10^9

	144	0.810	949	2.17	17.0	0.63	3347	6.10^{9}
	192	0.809	1020	2.37	17.9	0.59	3248	5.10^{9}
	240	0.810	1090	2.9	19.5	0.54	3016	9.10^{9}
A 316L SS	24	0.875	250	1.75	17.5	0.61	7865	3.10^{9}
	48	0.847	537	1.97	20.8	0.51	5256	4.10^{9}
	96	0.837	662	1.77	20.8	0.51	4836	2.10^{9}
	144	0.839	684	2.19	22.4	0.47	4696	5.10^{9}
	192	0.838	716	2.31	23.0	0.46	4505	5.10^{9}
	240	0.837	745	2.54	23.4	0.44	4394	6.10^{9}
B 316L SS	24	0.855	480	1.53	22.0	0.48	5032	2.10^{8}
	48	0.821	860	1.39	19.4	0.55	3774	4.10^{9}
	96	0.822	846	1.55	19.4	0.55	3759	7.10^{9}
	144	0.8221	840	1.63	19.3	0.55	3797	8.10^{9}
	192	0.822	866	1.68	19.9	0.53	3742	9.10^{9}
	240	0.823	884	1.75	20.7	0.51	3645	9.10^{9}

[a] Parameters obtained from a graphical analysis [64].
[b] Parameters obtained from Equations (5) and (7).
[c] Parameters obtained by the fitting.

CONCLUSION

This research work investigated the influence of feedstock powders on the microstructural properties and corrosion behaviour of L-PBF 316L SS. The corrosion performance of two materials (A 316L SS and B 316L SS) was evaluated and compared to the performance of a conventional wrought 316L SS in nitric acid at boiling temperature:

1) The A 316L SS shows microstructural properties typical of those expected for a L-PBF 316L SS. A heterogeneous and hierarchical structure is obtained with the presence of melt pool, columnar grains, a specific grain boundary distribution, solidification cells, dislocations and Mn and Si oxide precipitates. The B 316L SS has a similar heterogeneous and hierarchical structure. However, the microstructural properties of this steel present additionnaly many particularities. Firstly, the grain morphology is non-columnar due to an inhibition of epitaxial growth. More surprisingly, an internal cellular sub-network is organised within the large cells. The B 316L SS is then characterised by the presence of an unexpected triple structuration (grains, large cells, small internal cells). Another difference concerns the precipitates (Mn and Si oxides) which seem to be enriched in Cr contrary to the A 316L SS.
2) In corrosion, L-PBF 316L SS have shown better performance than wrought 316L SS. Different corrosion mechanisms were evinced depending on the material. For wrought 316L SS, uniform and intergranular corrosion appear leading to significant surface grain detachment and higher corrosion rates. For A 316L SS, two forms of localized corrosion occur. The first is

a moderate intergranular corrosion with intermediate intergranular penetration which does not lead to grain loss at the surface during the test period. The second is an intense cellular corrosion due to a galvanic coupling between large cell walls and the matrix. In contrast, B 316L SS shows an uniform dissolution and is distinguished by the absence of cell corrosion and a slightly intergranular attack. The enhanced resistance to cellular corrosion for this material is owing to the presence of the internal cellular sub-network which induces a homogenisation of the chemical composition (less Cr-depleted areas). The improvement in intergranular corrosion performance does not seem to be related to the nature and the electrochemical behaviour of the oxide film at the surface. However, considering the significant differences in solidification rates according to the process used, it is possible that the difference in the intergranular corrosion resistance is mainly related to the intrinsic properties of the grain boundaries with differences in local chemical composition.

MATERIALS AND METHODS

Powders and materials

Two different 316L SS powders were used, one provided by Oerlikon Metco (A) and the other by Praxair (B). During the manufacturing process of these powders, they were atomized under nitrogen and argon for A and B respectively. The chemical compositions of these powders were measured by inductively coupled plasma atomic emision spectrometry (ICP-AES) with an Optima 8300 DV (Perkin Elmer), glow discharge mass spectrometry with an Element GD Plus (Thermo Fisher) and by a O and N analyser Horiba EMGA-920. The chemical compositions are in accordance with standard (ASTM A240) and are presented in Table 3. A wrought 316L SS was also used as reference material in the corrosion study. The chemical composition of this conventionnal material is presented in Table 3.

Table 3: Chemical composition of the different 316L SS powder and the wrought 316L SS, in wt .%, used in this work.

Element	**Fe**	**Cr**	**Ni**	**Mn**	**Mo**	**Si**	**C**	**P**	**S**	**N**	**O**
Powder A	Bal.	17.3	12.9	1.1	2.1	0.38	<0.03	0.02	0.008	0.1	0.05
Powder B	Bal.	16.2	11.9	0,4	2.2	0.36	<0.03	0.005	0.006	0.01	0.04
Wrought 316L SS	Bal.	16.5	10.2	1.6	2.0	0.37	0.01	0.02	0.004	0.08	-
ASTM A240	Bal.	16-18	10-14	≤ 2	2-3	≤0.75	≤0.03	≤0.045	≤0.03	-	-

Additive manufacturing processing

In this work, the main objective was to compare the corrosion behavior of L-PBF 316L SS depending on the chosen raw material. The fabrication of the materials was performed using a Trumpf TruPrint Series 1000 printer, which is equipped with an Yb laser fiber with a wavelength of 1070 nm. A preliminary parametric study was carried out for the two materials A and B 316L SS in order to choose an adapted and optimal combination of parameters (density higher than 99%). The same laser power (120 W), laser spot diameter (30 µm), scanning strategy (stripes with 67° alternation between each layer), hatching distance (60 µm), powder bed thickness (30 µm) were used for both A and B 316L SS. However, different scanning speed values were used to obtain an almost equivalent density for A and B samples. The scanning speed for A 316L SS was 800 mm.s^{-1}, and 950 mm.s^{-1} for B 316L SS. For the A and B 316L SS, the optimal density obtained was 99.9% (determined by optical microscopy).

Microstructural characterization

The phase analyses were performed by X-ray Diffraction (XRD) using a Bruker D8 Advance diffractometer equipped. A Lynxeye linear detector used in 1D mode (energy discimination 0.19 - 0.25) and 2θ angle varying from 39° to 120° at ψ = 0°, φ = 90°, with a step of 0.03° and a time of 3 seconds per point were used.

An electrochemical etching was performed on the L-PBF 316L SS with an oxalic acid solution (10 wt.%) and observed by optical microscopy. The parameters applied by the power supply for the electrochemical etching were a voltage of 5 V and a current of 200 mA.

All observations made during the study were performed on surfaces which are parallel to the build direction of the L-PBF 316L SS. The grains morphology, the average grain size, the texture and the distribution of the grain boundaries of 316L SS were determined using a SEM-TESCAN VEGA 3 coupled to a Brucker Nano Quantax EBSD detector. The acquisition of the EBSD maps was achieved by applying an acceleration voltage of 20 kV and a working distance fixed at 16 mm. Prior to these analyses, samples were polished to a mirror-polished surface (diamond finish 1 µm) followed by OPS vibration polishing in order to remove the residual surface hardening.

Microstructure and composition of L-PBF 316L SS samples were investigated by transmission electron microscopy (TEM) using a Tecnai FEI F20 FEG-TEM (200kV accelerating voltage, sample tilted at 20°) coupled to a Bruker XFlash 6T | 60 EDS detector. For this purpose, thin sections were taken perpendicular to the build direction (machining of 3 mm diameter cylinders, cutting of disks of about 100 µm thickness and thinning with a solution of 45% butoxyethanol, 45% acetic acid, 10% perchloric acid at 0 °C with a voltage of 40 V). The observed areas correspond to the solidification cells with the <001> direction at ± 20° from the observation direction. Thin sections have also been observed by SEM, using a a Zeiss Cross-Beam 550 which is a FIB-SEM equipped with a SE and InLens detector. Finally, these images were obtained by applying an acceleration voltage of 5 kV, a working distance of 8 mm and a current of 1 nA.

Corrosion behaviour

- **Immersion test**

Immersion tests were performed in nitric acid HNO_3 (5 $mol.L^{-1}$) containing V(V) (4.10^{-3} $mol.L^{-1}$) at boiling temperature (107°C). The immersion tests consist in immersing the materials in a test medium and measuring their mass loss in order to determine their corrosion kinetics. For this purpose, 3 mirror-polished (diamond finish 1 µm) samples (2.8x2x0.65 cm^3) of each material were introduced into the reactor (2 L of solution). The total duration of the immersion test consisted of 5 periods of 48 h each (a total of 240 h). At the end of each period, the samples were cleaned with water and ethanol, dried, and then weighed and observed by optical microscopy. At the end of the 240 h of immersion, finer characterizations of corrosion morphologies and surface roughness were performed using a Zeiss ULTRA55 SEM FEG equipped with a secondary electron detector (accelerating voltage of 30 kV and working distance of 3 mm) and using a Brucker Contour GT-K optical profilometer (green illumination and processing method type vertical scanning interferometry). In addition, cross-sectional observations were carried out by optical microscopy in order to determine the attack depths and angles of the grain boundaries for the three steels. Finally, an analysis of the oxide layer on the extreme surface was performed by X-Ray Photo-electron Spectroscopy (XPS). The equipment used for these analyses was an Escalab 250 XI spectrometer equipped with a monochromatic X-ray Al-Kα source and an analysis spot with a diameter of 900 µm. The high-resolution spectra were recorded using a constant pass energy of 20 eV.

- **Electrochemical test**

A 3-electrode set-up was used with the material studied (wrought 316L SS, A 316L SS and B 316L SS) as the working electrode, a Pt grid as the counter electrode and a mercurous sulfate reference electrode (MSE, $Hg/Hg_2SO_4/K_2SO_4$ saturated, E_{ref} = 0.6513 V/SHE at 25°C). The reference electrode was protected from the acid solution and high temperature by a triple salt bridge. All measurements were performed with a Biologic VSP potentiostat controlled by the Ec-Lab software (BioLogic).

At the end of the 240 h of immersion, linear voltammetry measurements were performed in order to determine the corrosion potential (E_{corr}) and the corrosion current density (J_{corr}). To carry out these measurements, a linear potential sweep (scan rate of 0.2 $mV.s^{-1}$) was imposed from a starting potential (+ 30 mV/E_{OCP}) to a final potential (-0.600 V/E_{MSE}). Then, a linear potential sweep at the same scan rate was imposed from -30 mV/E_{OCP} to 0.700 V/E_{MSE}.

Potentiostatic electrochemical impedance spectroscopy (PEIS) measurements at open circuit potential (OCP) were performed after different immersion times (24 h, 48 h, 96 h, 144 h, 192 h and 240 h). A sinusoidal perturbation of 10 mV in a frequency domain ranging from 10 kHz to 10 mHz was applied.

Declaration of competing interest

The authors declare that they have no known competing financial interest or personal relationships that could have appeared to influence the work reported in this paper.

Credit authorship contribution statement

Alexis Fouchereau: Methodology, Validation, Investigation, Writing – original draft, Writing – review & editing, Visualization. **Hicham Maskrot:** Conceptualization, Writing – Review & editing, Supervision. **Fernando Lomello:** Conceptualization, Writing – review & editing, Supervision. **Sophie Bosonnet:** Conceptualization, Writing – review & editing, Supervision. **Oumaïma Gharbi:** Conceptualization, Writing – review & editing, Supervision. **Benoit Gwinner:** Conceptualization, Writing – review & editing, Supervision. **Pierre Laghoutaris:** Conceptualization, Project administration, Resources, Funding acquisition. **Frédéric Schuster:** Conceptualization, Project administration, Resources, Funding acquisition. **Vincent Vivier:** Conceptualization, Writing – review & editing, Supervision. **Beatriz Puga:** Conceptualization, Writing – review & editing, Supervision.

Acknowledgments

The authors gratefully acknowledge the CEA Cross-Cutting Program on Materials and Processes Skills for the technical and financial support. The authors gratefully acknowledge also S. Depinoy from the Centre of materials of Mines ParisTech in France for the technical support of TEM analyses, F. Miserque from the CEA in France for the technical support of XPS analyses and Hélène Isnard from the CEA in France for the technical support of ICP-AES, GDMS analyses. Finally, the authors acknowledge financial support from the CEA « MATER » and « ASMAT » projects.

REFERENCES

[1] I. Gibson, D.W. Rosen, B. Stucker, Additive Manufacturing Technologies, Springer US, Boston, MA, (2010). http://link.springer.com/10.1007/978-1-4419-1120-9

[2] K. Rajaguru, T. Karthikeyan, V. Vijayan, Additive manufacturing – State of art, Mater. Today Proc. 21 (2020) 628–633. https://doi.org/10.1016/j.matpr.2019.06.728.

[3] T.D. Ngo, A. Kashani, G. Imbalzano, K.T.Q. Nguyen, D. Hui, Additive manufacturing (3D printing): A review of materials, methods, applications and challenges, Compos. Part B Eng. 143 (2018) 172–196. https://doi.org/10.1016/j.compositesb.2018.02.012.

[4] T. Delacroix, F. Lomello, F. Schuster, H. Maskrot, J.-P. Garandet, Influence of powder recycling on 316L stainless steel feedstocks and printed parts in laser powder bed fusion, Addit. Manuf. 50 (2022) 102553. https://doi.org/10.1016/j.addma.2021.102553.

[5] F. Ahmed, U. Ali, D. Sarker, E. Marzbanrad, K. Choi, Y. Mahmoodkhani, E. Toyserkani, Study of powder recycling and its effect on printed parts during laser powder-bed fusion of 17-4 PH stainless steel, J. Mater. Process. Technol. 278 (2020) 116522. https://doi.org/10.1016/j.jmatprotec.2019.116522.

[6] N.E. Gorji, R. O'Connor, A. Mussatto, M. Snelgrove, P.G.M. González, D. Brabazon, Recyclability of stainless steel (316 L) powder within the additive manufacturing process, Materialia. 8 (2019) 100489. https://doi.org/10.1016/j.mtla.2019.100489.

[7] C.Y. Yap, C.K. Chua, Z.L. Dong, Z.H. Liu, D.Q. Zhang, L.E. Loh, S.L. Sing, Review of selective laser melting: Materials and applications, Appl. Phys. Rev. 2 (2015) 041101. https://doi.org/10.1063/1.4935926.

[8] C. Pauzon, E. Hryha, P. Forêt, L. Nyborg, Effect of argon and nitrogen atmospheres on the properties of stainless steel 316 L parts produced by laser-powder bed fusion, Mater. Des. 179 (2019) 107873. https://doi.org/10.1016/j.matdes.2019.107873.

[9] T. Delacroix, F. Lomello, F. Schuster, H. Maskrot, C. Baslari, U. Gaumet, Y. Flici, J.-P. Garandet, Influence of build characteristics and chamber oxygen concentration on powder degradation in laser powder bed fusion, Powder Technol. 416 (2023) 118231. https://doi.org/10.1016/j.powtec.2023.118231.

[10] AlMangour, Additive Manufacturing of High-Performance 316L Stainless Steel Nanocomposites via SLM, UCLA Electronic Theses and Dissertations, University of California (2017), https://escholarship.org/uc/item/4jp76591.

[11] A. Leicht, U. Klement, E. Hryha, Effect of build geometry on the microstructural development of 316L parts produced by additive manufacturing, Mater. Charact. 143 (2018) 137–143. https://doi.org/10.1016/j.matchar.2018.04.040.

[12] H.J. Niu, I.T.H. Chang, Instability of scan tracks of selective laser sintering of high speed steel powder, Scr. Mater. 41 (1999) 1229–1234. https://doi.org/10.1016/S1359-6462(99)00276-6.

[13] S. Das, Physical Aspects of Process Control in Selective Laser Sintering of Metals, Adv. Eng. Mater. 5 (2003) 701–711. https://doi.org/10.1002/adem.200310099.

[14] K.G. Prashanth, S. Scudino, T. Maity, J. Das, J. Eckert, Is the energy density a reliable parameter for materials synthesis by selective laser melting?, Mater. Res. Lett. 5 (2017) 386–390. https://doi.org/10.1080/21663831.2017.1299808.

[15] Z. Sun, X. Tan, S.B. Tor, W.Y. Yeong, Selective laser melting of stainless steel 316L with low porosity and high build rates, Mater. Des. 104 (2016) 197–204. https://doi.org/10.1016/j.matdes.2016.05.035.

[16] J.A. Cherry, H.M. Davies, S. Mehmood, N.P. Lavery, S.G.R. Brown, J. Sienz, Investigation into the effect of process parameters on microstructural and physical properties of 316L stainless steel parts by selective laser melting, Int. J. Adv. Manuf. Technol. 76 (2015) 869–879. https://doi.org/10.1007/s00170-014-6297-2.

[17] S. Luisa, N. Contuzzi, A. Angelastro, A. Domenico, Capabilities and Performances of the Selective Laser Melting Process, in: M. Joo (Ed.), New Trends Technol. Devices Comput. Commun. Ind. Syst., Sciyo, 2010. https://doi.org/10.5772/10432.

[18] A. Eliasu, A. Czekanski, S. Boakye-Yiadom, Effect of laser powder bed fusion parameters on the microstructural evolution and hardness of 316L stainless steel, Int. J. Adv. Manuf. Technol. 113 (2021) 2651–2669. https://doi.org/10.1007/s00170-021-06818-9.

[19] G. Sander, A.P. Babu, X. Gao, D. Jiang, N. Birbilis, On the effect of build orientation and residual stress on the corrosion of 316L stainless steel prepared by selective laser melting, Corros. Sci. 179 (2021) 109149. https://doi.org/10.1016/j.corsci.2020.109149.

[20] B.M. Morrow, T.J. Lienert, C.M. Knapp, J.O. Sutton, M.J. Brand, R.M. Pacheco, V. Livescu, J.S. Carpenter, G.T. Gray, Impact of Defects in Powder Feedstock Materials on Microstructure of 304L and 316L Stainless Steel Produced by Additive Manufacturing, Metall. Mater. Trans. A. 49 (2018) 3637–3650. https://doi.org/10.1007/s11661-018-4661-9.

[21] M.J. Heiden, L.A. Deibler, J.M. Rodelas, J.R. Koepke, D.J. Tung, D.J. Saiz, B.H. Jared, Evolution of 316L stainless steel feedstock due to laser powder bed fusion process, Addit. Manuf. 25 (2019) 84–103. https://doi.org/10.1016/j.addma.2018.10.019.

[22] E. de Sonis, S. Dépinoy, P.-F. Giroux, H. Maskrot, L. Lemarquis, O. Hercher, F. Villaret, A.-F. Gourgues-Lorenzon, Dependency of recrystallization kinetics on the solidification microstructure of 316L stainless steel processed by laser powder bed fusion (LPBF), Mater. Charact. 194 (2022) 112370. https://doi.org/10.1016/j.matchar.2022.112370.

[23] L. Lemarquis, P.F. Giroux, H. Maskrot, B. Barkia, O. Hercher, P. Castany, Cold-rolling effects on the microstructure properties of 316L stainless steel parts produced by Laser Powder Bed Fusion (LPBF), J. Mater. Res. Technol. 15 (2021) 4725–4736. https://doi.org/10.1016/j.jmrt.2021.10.077.

[24] A.T. Sutton, C.S. Kriewall, M.C. Leu, J.W. Newkirk, Powder characterisation techniques and effects of powder characteristics on part properties in powder-bed fusion processes, Virtual Phys. Prototyp. 12 (2017) 3–29. https://doi.org/10.1080/17452759.2016.1250605.

[25] R. Li, Y. Shi, Z. Wang, L. Wang, J. Liu, W. Jiang, Densification behavior of gas and water atomized 316L stainless steel powder during selective laser melting, Appl. Surf. Sci. 256 (2010) 4350–4356. https://doi.org/10.1016/j.apsusc.2010.02.030.

[26] M.Z. Gao, B. Ludwig, T.A. Palmer, Impact of atomization gas on characteristics of austenitic stainless steel powder feedstocks for additive manufacturing, Powder Technol. 383 (2021) 30–42. https://doi.org/10.1016/j.powtec.2020.12.005.

[27] A. Chniouel, Study of 316L stainless steel processed by selective laser melting : influence of process parameters, powder characteristics, and heat treatments on the microstructure and mechanical properties, Thesis at University Paris Saclay (2019). https://theses.hal.science/tel-02421550.

[28] A. Leicht, M. Rashidi, U. Klement, E. Hryha, Effect of process parameters on the microstructure, tensile strength and productivity of 316L parts produced by laser powder bed fusion, Mater. Charact. 159 (2020) 110016. https://doi.org/10.1016/j.matchar.2019.110016

[29] M. Godec, S. Zaefferer, B. Podgornik, M. Šinko, E. Tchernychova, Quantitative multiscale correlative microstructure analysis of additive manufacturing of stainless steel 316L processed by selective laser melting, Mater. Charact. 160 (2020) 110074. https://doi.org/10.1016/j.matchar.2019.110074.

[30] Y. Song, Q. Sun, K. Guo, X. Wang, J. Liu, J. Sun, Effect of scanning strategies on the microstructure and mechanical behavior of 316L stainless steel fabricated by selective laser melting, Mater. Sci. Eng. A. 793 (2020) 139879. https://doi.org/10.1016/j.msea.2020.139879.

[31] X. Lou, M. Song, P.W. Emigh, M.A. Othon, P.L. Andresen, On the stress corrosion crack growth behaviour in high temperature water of 316L stainless steel made by laser powder bed fusion additive manufacturing, Corros. Sci. 128 (2017) 140–153. https://doi.org/10.1016/j.corsci.2017.09.017.

[32] M. Laleh, A.E. Hughes, S. Yang, J. Li, W. Xu, I. Gibson, M.Y. Tan, Two and three-dimensional characterisation of localised corrosion affected by lack-of-fusion pores in 316L stainless steel produced by selective laser melting, Corros. Sci. 165 (2020) 108394. https://doi.org/10.1016/j.corsci.2019.108394.

[33] G. Sander, J. Tan, P. Balan, O. Gharbi, D.R. Feenstra, L. Singer, S. Thomas, R.G. Kelly, J.R. Scully, N. Birbilis; Corrosion of Additively Manufactured Alloys: A Review. CORROSION 1 December 2018; 74 (12): 1318–1350. https://doi.org/10.5006/2926

[34] Leon, Avi & Aghion, Eli. (2017). Effect of surface roughness on corrosion fatigue performance of AlSi10Mg alloy produced by Selective Laser Melting (SLM). Materials Characterization. 131. https://doi.org/10.1016/j.matchar.2017.06.029

[35] K. Antony et S. Prasad Murugan, A Comparison of Corrosion Resistance of Stainless Steel Fabricated with Selective Laser Melting and Conventional Processing, International Journal of ChemTech Research (2014) 2632-2635.

[36] Kale, Amol & Kim, Byung-Kyu & Kim, Dong-Ik & Castle, E.G. & Reece, M. & Choi, S.-H., An investigation of the corrosion behavior of 316L stainless steel fabricated by SLM and SPS techniques. Materials Characterization. 163. 110204. (2020). https://doi.org/10.1016/j.matchar.2020.110204.

[37] F. Andreatta, A. Lanzutti, E. Vaglio, G. Totis, M. Sortino, L. Fedrizzi, Corrosion behaviour of 316L stainless steel manufactured by selective laser melting, Mater. Corros. 70 (2019) 1633–1645. https://doi.org/10.1002/maco.201910792.

[38] G. Sander, S. Thomas, V. Cruz, M. Jurg, N. Birbilis, X. Gao, M. Brameld, C.R. Hutchinson, On The Corrosion and Metastable Pitting Characteristics of 316L Stainless Steel Produced by Selective Laser Melting, J. Electrochem. Soc. (2017) 9. https://doi.org/10.1149/2.0551706jes

[39] Z. Duan, C. Man, C. Dong, Z. Cui, D. Kong, L. wang, X. Wang, Pitting behavior of SLM 316L stainless steel exposed to chloride environments with different aggressiveness: Pitting mechanism induced by gas pores, Corros. Sci. 167 (2020) 108520. https://doi.org/10.1016/j.corsci.2020.108520.

[40] A. Hemmasian Ettefagh, S. Guo, Electrochemical behavior of AISI316L stainless steel parts produced by laser-based powder bed fusion process and the effect of post annealing process, Addit. Manuf. 22 (2018) 153–156. https://doi.org/10.1016/j.addma.2018.05.014.

[41] Lodhi, M. Jahangir & Deen, Kashif Mairaj & Greenlee-Wacker, Mallary & Haider, Waseem, Additively manufactured 316L stainless steel with improved corrosion resistance and biological response for biomedical applications. Additive Manufacturing. (2019). 27. https://doi.org/10.1016/j.addma.2019.02.005.

[42] V.B. Vukkum, R.K. Gupta, Review on corrosion performance of laser powder-bed fusion printed 316L stainless steel: Effect of processing parameters, manufacturing defects, post-processing, feedstock, and microstructure, Mater. Des. 221 (2022) 110874. https://doi.org/10.1016/j.matdes.2022.110874.

[43] Rebecca F. Schaller, Ajit Mishra, Jeffrey M. Rodelas, Jason M. Taylor, Eric J. Schindelholz, The Role of Microstructure and Surface Finish on the Corrosion of Selective Laser Melted 304L, J. Electrochem. Soc. 165. (2018). https://doi.org/10.1149/2.0431805jes

[44] B. Puga, F. Lomello, E. Boussac, A. Chniouel, A. Fouchereau, P. Laghoutaris, H. Maskrot, « Influence of laser powder bed fusion processing parameters on corrosion behaviour of 316L stainless steel in nitric acid », Metallurgical Research & Technology 119 (5), 523 (2022) https://doi.org/10.1051/metal/2022079

[45] P. Fauvet, Corrosion issues in nuclear fuel reprocessing plants, in: Nucl. Corros. Sci. Eng., Elsevier, 2012: pp. 679–728. https://doi.org/10.1533/9780857095343.5.679.

[46] E. Tcharkhtchi-Gillard, Passivity and passivity breakdown of 304L stainless steel in hot and concentrated nitric acid, Thesis at University Pierre et Marie Curie (2014) 157. https://theses.hal.science/tel-01020901

[47] A. Emery, Intergranular corrosion mechanism of stainless steel (304L, Uranus 65) in nitric media, Thesis at University PSL, Mines ParisTech (2020) 163.

[48] E. Bardal, Corrosion and protection. London ; New York: Springer, (2004). https://doi.org/10.1007/b97510

[49] F. Balbaud, G. Sanchez, P. Fauvet, G. Santarini, G. Picard, Mechanism of corrosion of AISI 304L stainless steel in the presence of nitric acid condensates, Corros. Sci. 42 (2000) 1685–1707. https://doi.org/10.1016/S0010-938X(00)00021-4.

[50] B. Gwinner, M. Auroy, F. Balbaud-Célérier, P. Fauvet, N. Larabi-Gruet, P. Laghoutaris, R. Robin, Towards a reliable determination of the intergranular corrosion rate of austenitic stainless steel in oxidizing media, Corros. Sci. 107 (2016) 60–75. https://doi.org/10.1016/j.corsci.2016.02.020.

[51] A.F. Padilha, C.F. Tavares, M.A. Martorano, Delta Ferrite Formation in Austenitic Stainless Steel Castings, Mater. Sci. Forum. 730–732 (2012) 733–738. https://doi.org/10.4028/www.scientific.net/MSF.730-732.733.

[52] Q. Wang, S. Chen, L. Rong, δ-Ferrite Formation and Its Effect on the Mechanical Properties of Heavy-Section AISI 316 Stainless Steel Casting, Metall. Mater. Trans. A. 51 (2020) 2998–3008. https://doi.org/10.1007/s11661-020-05717-0.

[53] M. Laleh, A.E. Hughes, W. Xu, I. Gibson, M.Y. Tan, Corrosion behaviour of additively manufactured type 316L stainless steel, in Proceedings of the 2019 Australasian Conference on Corrosion & Prevention, Australasian Corrosion Association, Kerrimuir, Vic., (2019) 10.

[54] Y.M. Wang, T. Voisin, J.T. McKeown, J. Ye, N.P. Calta, Z. Li, Z. Zeng, Y. Zhang, W. Chen, T.T. Roehling, R.T. Ott, M.K. Santala, P.J. Depond, M.J. Matthews, A.V. Hamza, T. Zhu, Additively manufactured hierarchical stainless steels with high strength and ductility, Nat. Mater. 17 (2018) 63–71. https://doi.org/10.1038/nmat5021.

[55] F. Yan, W. Xiong, E. Faierson, Grain Structure Control of Additively Manufactured Metallic Materials, Materials. 10 (2017) 1260. https://doi.org/10.3390/ma10111260.

[56] D. Kong, C. Dong, S. Wei, X. Ni, L. Zhang, R. Li, L. Wang, C. Man, X. Li, About metastable cellular structure in additively manufactured austenitic stainless steels, Addit. Manuf. 38 (2021) 101804. https://doi.org/10.1016/j.addma.2020.101804.

[57] T. Voisin, J.-B. Forien, A. Perron, S. Aubry, N. Bertin, A. Samanta, A. Baker, Y.M. Wang, New insights on cellular structures strengthening mechanisms and thermal stability of an austenitic stainless steel fabricated by laser powder-bed-fusion, Acta Mater. 203 (2021) 116476. https://doi.org/10.1016/j.actamat.2020.11.018.

[58] D.J. Sprouster, W. Streit Cunningham, G.P. Halada, H. Yan, A. Pattammattel, X. Huang, D. Olds, M. Tilton, Y.S. Chu, E. Dooryhee, G.P. Manogharan, J.R. Trelewicz, Dislocation microstructure and its influence on corrosion behavior in laser additively manufactured 316L stainless steel, Addit. Manuf. 47 (2021) 102263. https://doi.org/10.101/j.addma.2021.102263.

[59] Mengkun Tian, Jahnavi Desai Choundraj, Thomas Voisin, Y. Morris Wang, Josh Kacher, Discovering the nanoscale origins of localized corrosion in additive manufactured stainless steel 316L by liquid cell transmission electron microscopy, Corrosion Science,Vol. 208 (2022). https://doi.org/10.1016/j.corsci.2022.110659.

[60] R.I. Revilla, J. Liang, S. Godet, I.D. Graeve, Local Corrosion Behavior of Additive Manufactured AlSiMg Alloy Assessed by SEM and SKPFM, J. Electrochem. Soc. (2017) 10. https://doi.org/10.1149/2.0461702jes

[61] B. Laurent, Corrosion behavior of a silicon enriched austenitic stainless steel in hot and concentrated nitric acid media, Thesis at University PSL (2017) 275.

[62] G.J. Brug, A.L.G. van den Eeden, M. Sluyters-Rehbach, J.H. Sluyters, The analysis of electrode impedances complicated by the presence of a constant phase element, J. Electroanal. Chem. Interfacial Electrochem. 176 (1984) 275–295. https://doi.org/10.1016/S0022-0728(84)80324-1.

[63] M. Orazem, B. Tribollet, Electrochemical Impedance Spectroscopy (Second Edition). (2017). https://doi.org/10.1002/9781119363682

[64] M.E. Orazem, N. Pébère, B. Tribollet, Enhanced Graphical Representation of Electrochemical Impedance Data, J. Electrochem. Soc. 153 (2006) B129. https://doi.org/10.1149/1.2168377.

[65] B. Hirschorn, M.E. Orazem, B. Tribollet, V. Vivier, I. Frateur, M. Musiani, Constant-Phase-Element Behavior Caused by Resistivity Distributions in Films, J. Electrochem. Soc. 157 (2010) C458. https://doi.org/10.1149/1.3499565.

[66] M.E. Orazem, B. Tribollet, V. Vivier, D.P. Riemer, E. White, A. Bunge, On the Use of the Power-Law Model for Interpreting Constant-Phase-Element Parameters, J. Braz. Chem. Soc. (2014). https://doi.org/10.5935/0103-5053.20140021.

[67] B. Lovreček, J. Sefaja, Semiconducting aspects of the passive layer on chromium, Electrochimica Acta, Vol. 17. (1972) 1151-1155. https://doi.org/10.1016/0013-4686(72)90031-X.

[68] B. Hirschorn, M.E. Orazem, B. Tribollet, V. Vivier, I. Frateur, M. Musiani, Determination of effective capacitance and film thickness from constant-phase-element parameters, Electrochimica Acta. 55 (2010) 6218–6227. https://doi.org/10.1016/j.electacta.2009.10.065.

[69] M.E. Orazem, I. Frateur, B. Tribollet, V. Vivier, S. Marcelin, N. Pébère, A.L. Bunge, E.A. White, D.P. Riemer, M. Musiani, Dielectric Properties of Materials Showing Constant-Phase-Element (CPE) Impedance Response, J. Electrochem. Soc. 160 (2013) C215–C225. https://doi.org/10.1149/2.033306jes.